Hole Contacts on Transition Metal Dichalcogenides: Interface Chemistry and Band Alignments

Stephen McDonnell,[†,*] Angelica Azcatl,[†] Rafik Addou,[†] Cheng Gong,[†] Corsin Battaglia,[‡] Steven Chuang,[‡] Kyeongjae Cho,[†] Ali Javey,[‡] and Robert M. Wallace[†,*]

[†]Department of Materials Science and Engineering, The University of Texas at Dallas, Richardson, Texas 75080, United States, and [‡]Electrical Engineering and Computer Sciences, University of California, Berkeley, California 94720, United States

ABSTRACT MoO_x shows promising potential as an efficient hole injection layer for p-FETs based on transition metal dichalcogenides. A combination of experiment and theory is used to study the surface and interfacial chemistry, as well as the band alignments for MoO_x/MoS_2 and MoO_x/WSe_2 heterostructures, using photoelectron spectroscopy, scanning tunneling microscopy, and density functional theory. A Mo^{5+} rich interface region is identified and is proposed to explain the similar low hole Schottky barriers reported in a recent device study utilizing MoO_x contacts on MoS_2 and WSe_2.

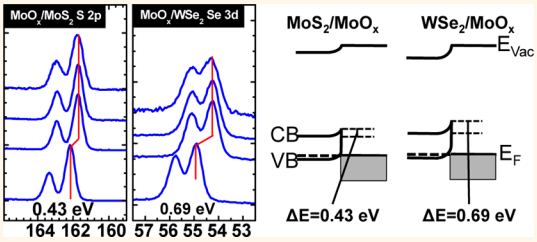

KEYWORDS: TMDs · MoS_2 · WSe_2 · band bending · X-ray photoelectron spectroscopy · hole contacts

Since the initial isolation[1] of stable monolayers exfoliated from 2D crystals such as graphite and MoS_2, significant efforts have been undertaken to integrate such low dimensional materials into nanoelectronic device architectures.[2−6] Transition metal dichalcogenides (TMDs) have been identified as attractive 2D alternatives to graphene since many of these materials possess bandgaps which can be tuned by the appropriate choice of metal or chalcogen as well as thickness.[7] Achieving low resistance contacts with these materials has been identified as a requirement to realizing TMD based nanoelectronic devices.[8,9]

For MoS_2, it is known that metal contacts typically exhibit low electron Schottky barriers even when the metals employed have a large work function close to the MoS_2 valence band (*e.g.*, Au 5.1 eV).[10] This phenomenon has recently been attributed to intrinsic defects in MoS_2 cleaned by mechanical exfoliation.[11] For complementary metal-oxide-semiconductor (CMOS) logic applications, it is important to find contacts that provide low Schottky barriers for hole injection to enable p-type field effect transistors (p-FETs). Our recent work identified thermally evaporated substoichiometric MoO_x ($x < 3$) as an efficient hole contact for MoS_2 and WSe_2, enabling the first realization of MoS_2 p-FETs and improving current injection into WSe_2 p-FETs.[12] MoO_x possesses a very high work function exceeding those of elemental metals.[13] The nonstoichiometric nature of MoO_x, caused by an oxygen deficiency, allows the formation of defect states within the band gap[14,15] resulting in metal-like behavior having a high work function and low density of states at the Fermi level. The MoO_x hole injection barrier to MoS_2 and WSe_2 substrates was shown to be lower than that of elemental high work function metals such as Pd or Au.[12]

A recent study investigated the influence of a MoO_x overlayer on the channel of MoS_2 n-FETs resulting in the depletion of the channel due to charge transfer, but no p-type transport behavior was reported.[16] The chemistry of the MoO_x/TMD hole contact interface, as well as the exact band alignment, is not yet understood. In this study, the details of the device relevant interface chemistry and band bending for MoO_x/MoS_2 and MoO_x/WSe_2 heterostructures are investigated.

Natural MoS_2 and WSe_2 crystals were purchased from SPI supplies[17] and Nanoscience,[18] respectively. These samples were cleaned by mechanical exfoliation using Scotch tape to remove the topmost layers

* Address correspondence to stephenmcd@utdallas.edu, rmwallace@utdallas.edu.

Received for review March 29, 2014 and accepted May 5, 2014.

Published online May 05, 2014
10.1021/nn501728w

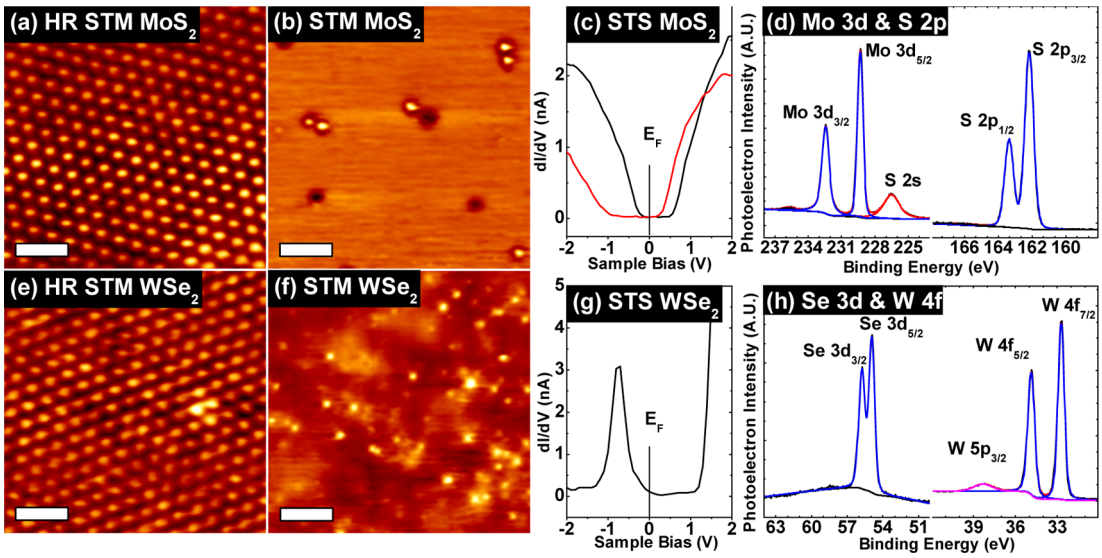

Figure 1. Initial MoS_2 (a–d) and WSe_2 (e–h) characterization. (a and e) High-resolution STM showing the atomic structure, scale bar 1 nm, imaging conditions (a) 0.7 V, 1 nA, and (e) 1.5 V, 1.5 nA. (b and f) 60 nm × 60 nm image showing that both surfaces are defective, scale bar 12 nm, imaging conditions (b) −0.3 V, 0.1 nA, and (f) 0.5 V, 1.3 nA. (c and g) STS spectra showing typical n- and p-type variability of MoS_2, and typically p-type behavior of WSe_2. (d and h) XPS of the initial surfaces showing the expected MoS_2 and WSe_2 chemical states.

of the bulk crystals. The two samples were mounted on a single plate and loaded, less than 5 min after exfoliation, into an ultra high vacuum (UHV) system. As such, both samples saw identical processing conditions and the MoO_x deposition was carried out simultaneously on the MoS_2 and WSe_2 crystals. Sequential depositions were carried out so that the interface evolution could be monitored as a function of MoO_x thickness by *in situ* X-ray photoelectron spectroscopy (XPS). The initial atomic structures and local spectroscopic properties of MoS_2 and WSe_2 surfaces were investigated using scanning tunneling microscopy (STM) and spectroscopy (STS), respectively, and an Omicron VT-STM operating at a base pressure of 2×10^{-10} mbar. Given the extensive data acquisition time required for the STM/STS and the high work function sensitivity of MoO_x to adsorbed carbon contamination, STM/STS was not acquired sequentially after each deposition.[15]

With the use of binding energy shifts in the core-level spectra as a measure of the band bending at the interfaces, band alignment diagrams can be constructed for both heterostructures once the band structures for the MoS_2 and WSe_2 are known. We compare the results obtained using a combination of reports on experimentally determined bandgaps and photoionization energies to those obtained by independently calculating the structure. We apply first-principles density functional theory (DFT)[19] to study the surface electronic properties of these two crystals based on the energetically favorable trigonal prismatic structures.

RESULTS AND DISCUSSION

Initial Transition Metal Dichalcogenide Surfaces. The "as exfoliated" MoS_2 and WSe_2 samples were initially characterized by XPS, STM and STS. The details of the MoS_2 characterization have been reported in a recent study;[11] however, the key points pertaining to the MoS_2 surface condition shall be summarized here for completeness. The MoS_2 is known to exhibit both p- and n-type behavior, due to local variations in stoichiometry. Atomically resolved STM (Figure 1a) shows that the 2H-MoS_2 polytype is confirmed[20,21] by the hexagonal structure and the lattice parameter $a = 3.2 \pm 0.2$ Å. XPS analysis reveals that carbon is the only reproducibly detectable contaminant,[11,22] with oxygen only occasionally being observed near the limit of XPS detection. A large concentration (1–5% areal density) of both structural defects and areas of high conductivity are present on the surface as shown in Figure 1b. The metallic-like (bright) defects are >2.5 nm in diameter and are assumed to be clusters of sulfur vacancies. They are confirmed to be areas of high electron density since they appear dark in positive bias as shown in previous work.[11] These defects were identified as the likely cause for the low electron Schottky barriers observed for high work function metals deposited on MoS_2. The resultant contact actually consists of parallel conduction paths through both the metal/MoS_2 contact and the defect/MoS_2 contact.[11] Assuming that the defects behave as lower work function metals, even 0.3% areal density of such a defect was found to dominate the observed electron Schottky barrier height. The dark defects are structural in nature and can be attributed to a missing layer of MoS_2 (often a subsurface defect) from the measured height difference of ~0.7 nm. The p- and n-type variations can be observed from the Fermi level position obtained by STS and shown in Figure 1c. These spectra are typical STS curves obtained from different

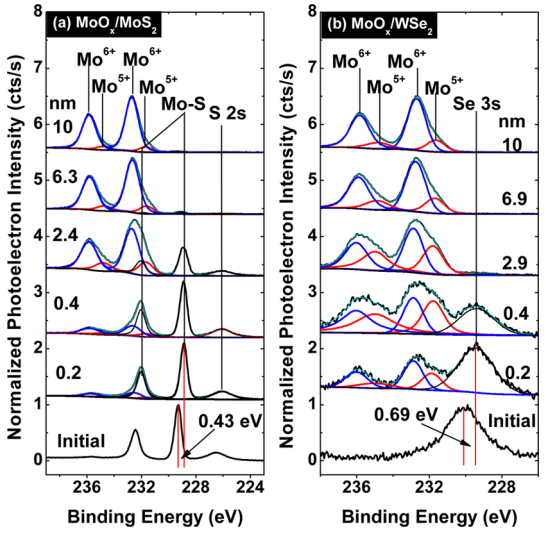

Figure 2. Evolution of the Mo 3d core level and the over lapping S 2s and Se 3s core levels for (a) MoO_x on MoS_2 and (b) MoO_x on WSe_2. The core-level spectra are acquired sequentially between MoO_x depositions of increasing thickness. The intensities have been normalized for the maximum intensity to facilitate visual comparison of the deconvolved spectra. Band bending of ~0.43 and 0.69 eV is observed in the MoS_2 and WSe_2, respectively, following the first deposition. With each deposition the MoO_x components (Mo^{5+} and Mo^{6+}) are seen to increase in intensity. Details of the fitting constraints employed for this spectral deconvolution are included in the Supporting Information.

areas of an MoS_2 sample. Both are acquired away from defects and local variations in the band gap are clearly observed. A detailed discussion on the correlation of such spectra with *I*−*V* measurements and XPS has been presented by McDonnell *et al.*[11] and it was shown that local variations in the material composition (ratio of Mo to S) can explain the local variations in the Fermi level position and band gap. As shown in Figure 1d, the initial spectra are indicative of p-type MoS_2.[11] The features in Figure 2a at 226.5, 229.3, and 232.4 eV are associated with the S 2s, Mo $3d_{5/2}$, and Mo $3d_{3/2}$ core levels in MoS_2, *i.e.*, Mo^{4+} and S^{2-} charge states due to S−Mo charge transfer. The feature at 235 eV could be attributed to the Mo $3d_{3/2}$ core level in the MoO_3 chemical state; however as discussed in previous work,[22] this feature is present even when oxygen is below the limit of detection and is therefore not assigned to an oxidation state in the initial spectra.

When the relative sensitivity factors of 2.867 for Mo 3d and 0.570 for S 2p are used,[23] it can be shown that the stoichiometry is 1.94, which is higher than the 1.7−1.8 that is typical for n-type MoS_2.[11]

The WSe_2 surface analyzed by STM (Figure 1e) is also hexagonal, with a lattice parameter of 3.3 ± 0.25 Å. From the 60 nm × 60 nm image shown in Figure 1f, the surface was found to also exhibit bright spots, however the nature of the bright spots appears to be quite different from MoS_2. Instead of observing both metallic like and structural defects, only structural defects are observed. Unlike the MoS_2, the bright features do not appear to clusters of Se vacancies. In fact these regions have an identical atomic structure to the flat regions of the surface when imaged with atomic resolution and appear bright even when imaged under positive bias. Figure 1g shows that the Fermi level position is typically located near the valence band edge and the band gap is ~1.2 eV as expected. It should be noted that the WSe_2 also shows some variability in the observed density of states, presumably related to surface defects (see the Supporting Information Figure S1), however the Fermi level is reproducibly found to be ~1.1 ± 0.1 eV below the conduction band edge. Figure 1h shows the core-level features obtained by XPS. The Se $3d_{5/2}$ and Se $3d_{3/2}$ core levels are observed at 54.9 and 55.8 eV, respectively. The W $4f_{7/2}$, W $4f_{5/2}$ and W $5p_{3/2}$ are observed at 32.7, 34.9, and 38.1 eV respectively. These values are consistent with those previously reported for WSe_2.[24,25]

MoO_x Depositions of MoS_2 and WSe_2. X-ray photoelectron spectroscopy was used to monitor the evolution of the interface chemistry for both of these samples as a function of MoO_x thickness as MoO_x was deposited incrementally. The samples were positioned within 5 mm of each other and as such both samples are assumed to have been exposed to an identical flux of MoO_x during the depositions. The thickness of the deposited MoO_x was calculated for both samples based on the attenuation of the S 2p and Se 3d core levels, using the NIST EAL Database[26] to derive the electron attenuation lengths for these core levels in MoO_x. The resultant thicknesses of (i) 0.2 nm, (ii) 0.4 nm, (iii) 2.4 nm, (iv) 6.3 nm, and (v) ~10 nm were obtained for the MoO_x film on MoS_2. The thicknesses for the MoO_x film on WSe_2 were calculated using the attenuation of the Se 3d core level and resulted in values of (i) 0.2 nm, (ii) 0.4 nm, (iii) 2.9 nm, (iv) 6.9 nm, and (v) ~10 nm. In both cases, the signals from the S 2p and Se 3d core levels after the fifth deposition were too weak to accurately determine the peak areas. The thicknesses of the final films are extrapolated from a linear fit of thickness *vs* deposition time using the first four data points. Such thickness calculations assume that the substrate is uniformly covered. As will be discussed later, this is not strictly true for thin MoO_x on TMDs and as such these values serve only as estimates for the amount of MoO_x deposited.

Figure 2 shows the evolution of the Mo 3d core level as MoO_x is deposited on the MoS_2 and WSe_2 substrates. The initial spectra have been discussed in relation to Figure 1. It is clear that after the first MoO_x deposition, the substrate related core-level features shift to lower binding energy. For the MoS_2 features, this shift is 0.43 ± 0.05 eV, whereas for the WSe_2, this shift is 0.69 ± 0.05 eV. Such shifts can be correlated to Fermi level realignment between MoO_x and TMDs resulting in upward band bending. For the MoS_2, this value is significantly smaller than the 1.06 eV that was recently

TABLE 1. Core-Level Positions, Band Bending, and Full Width Half Maximum Variation for MoO_x/MoS_2 and MoO_x/WSe_2 Heterostructures[a]

					fwhm		
	Mo 3d (S 2p)	ΔE	W 4f (Se 3d)	ΔE	(i)	(ii)	(iii)
MoS_2	229.30 (162.17)	−0.43			0.58	0.61	0.72
WSe_2			32.72 (54.91)	−0.69	0.55	0.60	0.71

[a] All units are electronvolts (eV).

reported,[16] for MoO_3 deposited on n-type MoS_2. In contrast, in our present work, MoO_x has been deposited on p-type MoS_2, making the differences in band bending easy to account for assuming that the Fermi level position in the work of Lin *et al.*[16] was 0.63 eV (1.06−0.43 eV) closer to the conduction band. S 2p (shown in the Supporting Information Figure S2) and Mo 3d presented only S^{2-} and Mo^{4+} MoS_2 chemical states, with no additional chemical states other than Mo^{5+} and Mo^{6+} MoO_x states observed after MoO_x deposition. Se 3d and W 4f (shown in the Supporting Information Figure S3) presented only Se^{2-} and W^{4+} WSe_2 chemical states with no additional chemical states observed after MoO_x deposition.

A summary of these findings, as well as an observed change in fwhm of the substrate features with the first three MoO_x depositions, is presented in Table 1. The broadening of the substrate signals could be due to inhomogeneous surface potentials caused by nonuniform (island type) growth of MoO_x on MoS_2.[27] This is observed by atomic force microscopy that was carried on out on the final films *ex situ* (see Supporting Information Figure S4). Such 3D growth of nonreacting metals on 2D crystals is expected, as it has been previously reported for both graphite and MoS_2.[28,29]

As discussed in detail in our recent work, the Mo 3d core-level positions for MoO_2 and MoO_3 chemical states overlap significantly with the core-level positions for the MoS_2 chemical state.[22] Similar to that study, the oxidation on MoS_2 surface cannot be ruled out by analysis of the Mo 3d core-level feature only but can be inferred from the lack of new chemical states observed in the S 2p region (shown in the Supporting Information Figure S2). Similarly, no unique tungsten or selenium chemical states are identified after MoO_x depositions on WSe_2 (shown in the Supporting Information Figure S3).

From the Mo 3d core-level spectra, which are shown in Figure 2, it is clear that the MoO_x deposits as a mixture of Mo^{5+} and Mo^{6+} states. Also evident is that the ratio of Mo^{5+} to Mo^{6+} decreases with increasing thickness, which is tabulated in Table 2. Therefore, it should be expected that the electronic properties of this film might vary with thickness until a bulk value is reached. Also evident from Figure 2 is that relative intensities of the Mo^{5+} and Mo^{6+} features are substrate dependent, with MoO_x on WSe_2 exhibiting a higher Mo^{5+} concentration.

TABLE 2. Ratio of Mo^{5+} to Mo^{6+} in the Deposited MoO_x with Increasing Thickness[a]

	Mo^{5+}:Mo^{6+}				
	(i) ∼0.2 nm	(ii) ∼0.4 nm	(iii) ∼2.7 nm	(iv) ∼ 6.7 nm	(v) ∼10 nm
MoS_2	0.31	0.31	0.30	0.15	0.10
WSe_2	0.45	0.77	0.58	0.28	0.20

[a] Thicknesses are given as the approximate average of those calculated for MoO_x and MoS_2 and WSe_2. The spectral analysis that yielded these values is shown in the Supporting Information (Figure S6).

The Effect of MoO_x Composition on the Work Function. Previous studies have shown that the ratio of Mo^{5+} to Mo^{6+} is both thickness and substrate dependent, with thin films having higher Mo^{5+} concentrations also yielding lower work functions.[14,30] This is confirmed in our own comparative study where two MoO_x films of different thicknesses, and therefore initial work functions, were intentionally reduced by atomic hydrogen exposure to increase their respective Mo^{5+} concentrations. In both cases, this was found to result in a lowering of the sample work function. This study is also described in more detail in the Supporting Information (see Figure S5) and serves as confirmation that MoO_x workfunction decreases with increasing Mo^{5+} concentration.

Examining the Mo^{5+} to Mo^{6+} ratio for both substrates shows that the composition of this initial layer is notably different on MoS_2 with respect to WSe_2 (Table 2). Given that on the WSe_2 there is a significantly higher concentration of Mo^{5+} for equivalent thicknesses, we posit that the work function of the MoO_x at the MoO_x/WSe_2 interface is lower than that at the MoO_x/MoS_2 interface. Hole Schottky barriers that could normally be estimated by comparing the semiconductor Fermi level and valence band edge to the metal work function may not trend with the position of the TMD valence band edge for MoO_x/TMD contacts due to this substrate dependence of the MoO_x work function.

Band Structure of MoS_2 and WSe_2. To understand the observed band bending, a detailed knowledge of the band structure for bulk MoS_2 and WSe_2 is required. Previous experimental determinations of the photoionization energy ($E_{vacuum} - E_{valence\ band\ maximum}$) for MoS_2 and WSe_2 allowed for the electron affinities (χ_A) of $\chi_A = 4.07 \pm 0.35$ and 4.03 ± 0.15 eV to be inferred.[27] This was achieved by using literature values for the MoS_2 and WSe_2 bandgaps, estimated at the time of the study to be 1.4 ± 0.2 and 1.16 ± 0.05 eV.[27,31−33] The value for WSe_2 is in good agreement with the general consensus[6,34] that WSe_2 has a band gap of ∼1.2 eV, and is also in the 1.05−1.35 eV range of experimentally determined band gaps from WSe_2 crystals.[35−37]

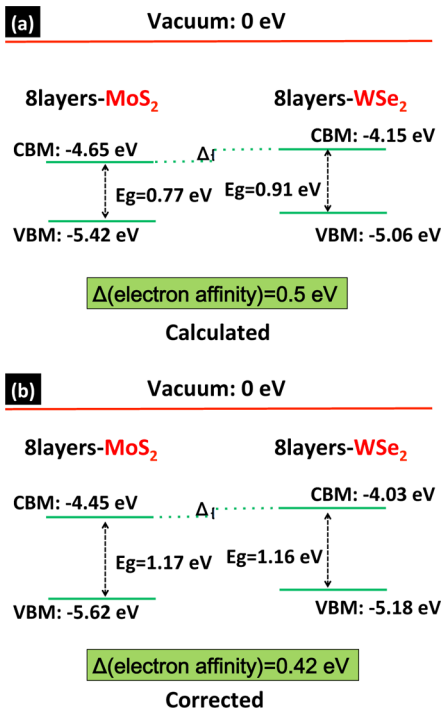

Figure 3. Conduction band and valence band positions for MoS_2 and WSe_2 relative to the vacuum level calculated within the local density approximation (LDA). The bandgaps in (a) are underestimated by LDA as expected; however, a clear energy difference between the electron affinity of MoS_2 and WSe_2 is observed. Expanding the bandgaps (b) symmetrically around the center of the bandgap to accepted experimental values, for both MoS_2 and WSe_2, leads to a decreased electron affinity difference of ~0.4 eV between MoS_2 and WSe_2.

However, the value of 1.4 eV for the MoS_2 band gap is significantly larger than the assumed values in more recent reports by Splendiani *et al.*[38] and Kim *et al.*[39] of 1 and 1.1 eV, respectively. It is also higher than the experimentally measured MoS_2 band gap by Kautek *et al.*[37] and McDonnell *et al.*[22] of 1.17 ± 0.03 and 1.23 ± 0.02 eV, respectively. As such, using the quoted values of χ_A = 4.07 and 4.03 ± 0.15 eV for MoS_2 and WSe_2, respectively, would not be correct. Here, we employ two independent methods for determining the band structure of the TMD materials.

To construct the conduction band a valence band points with respect to vacuum based on experiments, we combine the experimentally measured photoionization energies of MoS_2 and WSe_2 ($E_{\text{valence band maximum}}$ = 5.47 ± 0.15 and 5.19 ± 0.1 eV) by Schlaf *et al.*[27] with the experimentally measured band gaps (E_g = 1.17 ± 0.03 and 1.16 ± 0.03 eV) by Kautek *et al.*[37] This combination allows us to calculate electron affinities ($E_{\text{valence band maximum}} + E_g$) of 4.3 ± 0.15 and 4.03 ± 0.1 eV for MoS_2 and WSe_2, respectively. In subsequent discussions, deduced energy level positions based on these values will be referred to as "SK_{exp}."

First-principles calculations were also employed, the results of which are shown in Figure 3. The model

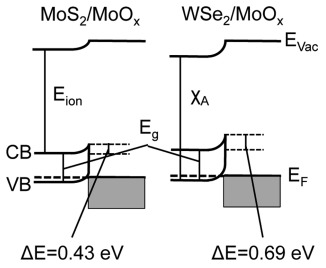

Figure 4. A simple schematic of the band lineup for the MoO_x/MoS_2 and MoO_x/WSe_2 heterostructures. These diagrams assume that the Fermi level position in WSe_2 is ~1.1 eV below the conduction band and the observed band bending is due the energy difference between the work function of the MoO_x and the initial Fermi level of the semiconducting substrate. This simple construction shows all the banding bending in the substrate similar to Schlaf *et al.*[27] The banding bending is obtained from the shifts observed in the XPS substrate features after the initial MoO_x deposition.

of the finite layers of TMDs is set by adding a vacuum region (~20 Å) normal to the surface. Eight layers are found to be enough for a reasonable reproduction of our calculated band gaps of the two bulk crystals (0.75 eV for bulk MoS_2, and 0.87 eV for bulk WSe_2, as shown in Figure 3). It is well-known that LDA tends to underestimate the band gaps of semiconductors. Instead of the absolute value of the band gap, the relative comparison of the electron affinity between MoS_2 and WSe_2 is the focus of this work. Calculated results in Figure 3 show that the electron affinity at the MoS_2 surface is 0.5 eV larger than that at the WSe_2 surface. Given the underestimation of the bandgap by LDA, we can crudely *ad hoc* correct these calculated electron affinities by assuming the midgap positions of the bandgaps are correct and symmetrically expanding the bands to match the experimental values[37] of 1.17 and 1.16 eV for MoS_2 and WSe_2, respectively. Doing so results in electron affinities for MoS_2 and WSe_2 of 4.45 and 4.03 eV, respectively. After this *ad hoc* correction, the calculated photoionizations of WSe_2 (5.2 eV) and MoS_2 (5.62 eV) are in agreement with the experimental values of Schlaf *et al.*[27] of 5.09−5.29 and 5.32−5.62 eV, respectively. In subsequent discussions, deduced energy level positions based on these numbers will be referred to as LDA.

Band Alignment in the MoO_x/MoS_2 and MoO_x/WSe_2 Heterostructures. With this information for the MoS_2 and WSe_2 band structures, the band alignments of the MoO_x/TMD heterostructures can be illustrated as shown in Figure 4, using the observed band bending and Fermi level position in WSe_2 taken from STS. This schematic shows that the MoO_x/MoS_2 and MoO_x/WSe_2 contacts with the Fermi levels aligned and illustrates the observed band banding. Also shown is that, due to the high work function of the MoO_x, the Fermi level at the interface lies below the valence band edge for both TMDs.

The measured and deduced energy level positions using both the LDA and SK_{exp} band structures for MoS_2

TABLE 3. Values for Band Bending (ΔE), Fermi Level Position (E_F), Band Gap (E_g), Photoionization Energy (E_{ion}), Electron Affinity (χ_A), and MoO_x Work Function (WF MoO_x) for the MoO_x/TMD Structures[a]

	ΔE	E_F	E_g	E_{ion}	χ_A	WF MoO_x
MoS_2(LDA)	0.43 ± 0.05*	5.56[A]	1.17 ± 0.03*	5.62[C]	4.45[C]	5.99 ± 0.05
MoS_2(SK_{exp})		5.41[A]		5.47 ± 0.15*	4.3 ± 0.15	5.84 ± 0.05
WSe_2(LDA)	0.69 ± 0.05*	5.13*	1.16 ± 0.03*	5.19[C]	4.03[C]	5.82 ± 0.05
WSe_2(SK_{exp})		5.13*		5.19 ± 0.1*	4.03 ± 0.1	5.82 ± 0.05

[a] Values are either experimentally measured (*), assumed ([A]), calculated by LDA ([C]), or deduced from the combination of the other values. Values for ΔE are measured from XPS, values for E_g are taken from Kautek *et al.*[37], and values for E_{ion} are taken from from Schlaf *et al.*[27].

and WSe_2 are shown in Table 3. Using the Fermi level position of p-type WSe_2 taken from the STS in Figure 1g to be ~0.06 eV above the valence band (*i.e.*, 0.06 lower energy than the photoionization potential), the work function of the MoO_x can be deduced by adding the measured 0.69 eV band bending at the MoO_x/WSe_2 interface. This work function may, in fact, be higher, since it is known that an interface dipole of up to 0.56 eV can exist at an MoO_3/MoS_2 interface.[16] More importantly, this minimum value of 5.82 eV is greater than the photoionization potentials of WSe_2 determined by LDA or SK_{exp}, and therefore, one would expect the resultant hole contacts to be Ohmic. The large variation in the local Fermi level position on MoS_2 samples makes a similar estimation using STS to determine the MoS_2 Fermi level position as well as the band bending to establish a minimum MoO_x work function impossible. The estimation of the band alignments shown in Figure 4 and quantified in Table 3 is based on the assumption that the initial Fermi level position of the p-type MoS_2 (suggested to be p-type based on the XPS binding positions) is 0.06 eV above the valence band maximum, similar to the WSe_2.

The work function of MoO_x has been previously reported[14,40] to be as high as 6.86 eV. However, the work function is also known to be highly sensitive to carbon concentration with values as low as 5.7 eV also being observed.[15] Moreover, the lowering of the MoO_x work function with increasing Mo^{5+} concentration suggests that the control of the initial interface stoichiometry, as well as carbon content, may be key to obtaining low resistance contacts. The key finding here is that the observed band bending on these p-type TMDs suggests that the work function of MoO_x should be sufficient to provide an Ohmic hole contact. It is clear that the observed trends are independent of the method (LDA *vs* SK_{exp}) used to obtain the TMD band structure information.

Correlation with Device Data. In both heterostructures, the constructed energy band diagrams suggest that the MoO_x should potentially make Ohmic hole contacts with both MoS_2 and WSe_2. In light of the recent work[12] showing hole Schottky barriers of 0.31 and 0.29 eV for the MoO_x/MoS_2 and MoO_x/WSe_2 contacts, respectively, an explanation for the presence of these barriers is required. This can readily be explained by a higher concentration of carbon being present in MoO_x that was deposited in high vacuum rather than UHV. It should also be noted that, given the difference in the experimentally measured photoionization energies[27] for MoS_2 and WSe_2 of 0.28 eV, the observation of almost identical hole Schottky barriers requires the work function of the contact metal at the TMD interface to be lower for WSe_2 than that for MoS_2. This can be explained due to the high Mo^{5+} concentration observed at the MoO_x/WSe_2 interface, noted in this present study, which is known to result in a lower work function MoO_x.

CONCLUSION

In summary, the evolution of the MoO_x/MoS_2 and MoO_x/WSe_2 interfaces during e-beam thermal evaporation of the MoO_x from MoO_3 powder in UHV has been studied by *in situ* XPS, STM, STS, and DFT. MoO_x was found to be deposited as substoichiometric oxide with $x < 3$ and with detectable defect states just below the Fermi level as expected. We found that, other than a broadening of the core-level features, no new substrate related chemical states were observed, suggesting that while there may be some nonuniform strain induced by the island growth, there are no detectable covalent bond formations. Upward band bending was observed for both MoS_2 and WSe_2, which is consistent with the expected ionization potentials of these TMDs and the known high work function of the MoO_x.

First principle calculations were employed to determine band structures of the MoS_2 and WSe_2 and were found to be in good agreement with values deduced from experimental photoionization energies and bandgaps. The combination of these band structures with the observed band bending in the MoO_x/MoS_2 and MoO_x/WSe_2 heterostructures allowed band alignments in each contact to be deduced.

A comparison with previously reported electrical data suggests that the band bending alone cannot wholly explain the observed hole Schottky barriers. We suggest that the discrepancy between these studies can be explained by the lower work function of MoO_x deposited *ex situ* in high vacuum, which has a higher spurious carbon concentration than that on UHV deposited MoO_x. Furthermore, the similar Schottky barriers observed on both MoS_2 and WSe_2, despite

the differences in their photoionization energies, can be explained by the higher Mo^{5+} concentration for MoO_x on WSe_2 relative to MoS_2 resulting in a lower work function than on MoS_2. These results suggest that control of the MoO_x purity and stoichiometry will be key in realizing the potential of MoO_x as an efficient Ohmic hole injection contact to many of the transition metal dichalcogenides.

MATERIALS AND METHODS

Stoichiometric MoO_3 powder was evaporated from an alumina-lined tungsten crucible heated by an electron beam, using a multipocket e-beam evaporator (Oxford Applied Research model EGC04). In this configuration, the electron beam impinges on the crucible rather than directly on the powder, and so the evaporation process is expected to be similar to thermal evaporation. The deposited material is known to be substoichiometric MoO_x. Prior to deposition, the MoO_x source was outgassed for several hours to minimize OH and carbon contamination. All depositions were performed on the crystals at room temperature with a working pressure of $\sim 2 \times 10^{-9}$ mbar.

The X-ray photoelectron spectrometer is equipped with a monochromated Al Kα source (hv =1486.7 eV) and an Omicron Argus detector operating with a pass energy of 15 eV. Core-level spectra are analyzed with the spectral analysis software Aanalyzer. The features were fit with Voigt line shapes, and an active Shirley background was used.[41]

To allow for XPS analysis where the X-ray spot size is approximately a 500 μm diameter, large crystals rather than isolated TMD flakes were utilized in this study. The MoS_2 and WSe_2 were $\sim 2 \times 8$ mm and 2×2 mm, respectively. Both crystals where $\gg$100 μm thick and as such can be assumed to exhibit bulk-like properties. An optical image of the samples is shown in the Supporting Information Figure S6.

Calculations for each TMD crystal are performed by VASP with the projector-augmented wave (PAW)[42] method. The local density approximation (LDA)[43] is used to describe the exchange-correlation functional, with the partial core correction included. During the ionic relaxation, both the size of the 1×1 unit cell and the positions of all constituent atoms are fully relaxed. The stopping criterion for the ionic relaxation is the remnant force on each atom below 0.01 eV/Å. The Monkhorst−Pack k-point sampling in the primitive Brillouin zone (BZ) is Γ-centered with $6 \times 6 \times 1$ and $20 \times 20 \times 1$ meshes in ionic and electronic optimization, respectively. The energy cutoff is chosen at 400 eV, and the electronic optimization stops when the total energies of neighboring optimization loops differ below 10^{-4} eV.

Conflict of Interest: The authors declare no competing financial interest.

Supporting Information Available: Additional information including details of the variation in the locally measured bandgap of WSe_2, additional XPS core-level spectra for MoO_x/MoS_2 and MoO_x/WSe_2, AFM evidence of the nonuniform MoO_x growth on MoS_2 and WSe_2, a detailed discussion of the variation of MoO_x work function as a function of Mo^{5+} concentration, and the details of spectral analysis of the Mo 3d core levels shown in Figure 2 that yield the Mo^{5+}:Mo^{6+} ratios tabulated in Table 2. This material is available free of charge *via* the Internet at http://pubs.acs.org.

Acknowledgment. The authors would like to thank Prof. Christopher Hinkle for useful discussions. This work was supported by the Center for Low Energy Systems Technology (LEAST), one of six centers supported by STARnet, a Semiconductor Research Corporation program sponsored by MARCO and DARPA.

REFERENCES AND NOTES

1. Novoselov, K.; Jiang, D.; Schedin, F.; Booth, T.; Khotkevich, V.; Morozov, S.; Geim, A. Two-Dimensional Atomic Crystals. *Proc. Natl. Acad. Sci. U.S.A.* **2005**, *102*, 10451–10453.
2. Fiori, G.; Iannaccone, G. Ultralow-Voltage Bilayer Graphene Tunnel FET. *IEEE Electron Device Lett.* **2009**, *30*, 1096–1098.
3. Banerjee, S. K.; Register, L. F.; Tutuc, E.; Reddy, D.; MacDonald, A. H. Bilayer Pseudospin Field-Effect Transistor (BISFET): A Proposed New Logic Device. *IEEE Electron Device Lett.* **2009**, *30*, 158–160.
4. Lin, Y. M.; Jenkins, K. A.; Valdes-Garcia, A.; Small, J. P.; Farmer, D. B.; Avouris, P. Operation of Graphene Transistors at Gigahertz Frequencies. *Nano Lett.* **2009**, *9*, 422–426.
5. Radisavljevic, B.; Radenovic, A.; Brivio, J.; Giacometti, V.; Kis, A. Single-Layer MoS_2 Transistors. *Nat. Nanotechnol.* **2011**, *6*, 147–150.
6. Fang, H.; Chuang, S.; Chang, T. C.; Takei, K.; Takahashi, T.; Javey, A. High-Performance Single Layered WSe_2 P-FETs with Chemically Doped Contacts. *Nano Lett.* **2012**, *12*, 3788–3792.
7. Wang, Q. H.; Kalantar-Zadeh, K.; Kis, A.; Coleman, J. N.; Strano, M. S. Electronics and Optoelectronics of Two-Dimensional Transition Metal Dichalcogenides. *Nat. Nanotechnol.* **2012**, *7*, 699–712.
8. Jena, D. Tunneling Transistors Based on Graphene and 2-D Crystals. *Proc. IEEE* **2013**, *101*, 1585–1602.
9. Seabaugh, A. C.; Zhang, Q. Low-Voltage Tunnel Transistors for Beyond CMOS Logic. *Proc. IEEE* **2010**, *98*, 2095–2110.
10. Das, S.; Chen, H.-Y.; Penumatcha, A. V.; Appenzeller, J. High Performance Multi-Layer MoS_2 Transistors with Scandium Contacts. *Nano Lett.* **2012**, 100–105.
11. McDonnell, S.; Addou, R.; Buie, C.; Wallace, R. M.; Hinkle, C. L. Defect Dominated Doping and Contact Resistance in MoS_2. *ACS Nano* **2014**, *8*, 2880–2888.
12. Chuang, S.; Battaglia, C.; Azcatl, A.; McDonnell, S.; Kang, J. S.; Yin, X.; Tosun, M.; Fang, H.; Kapadia, R.; Wallace, R. M.; *et al.* MoS_2 P-Type Transistors and Diodes Enabled by High Workfunction MoO_x Contacts. *Nano Lett.* **2014**, *14*, 1337–1342.
13. Michaelson, H. B. The Work Function of the Elements and Its Periodicity. *J. Appl. Phys.* **1977**, *48*, 4729–4733.
14. Greiner, M. T.; Lu, Z.-H. Thin-Film Metal Oxides in Organic Semiconductor Devices: Their Electronic Structures, Work Functions and Interfaces. *NPG Asia Mater.* **2013**, *5*, e55.
15. Battaglia, C.; Yin, X.; Zheng, M.; Sharp, I. D.; Chen, T. L.; Azcatl, A.; McDonnell, S.; Carraro, C.; Maboudian, R.; Wallace, R. M.; *et al.* Hole Selective MoO_x Contact for Silicon Solar Cells. *Nano Lett.* **2014**, *14*, 967–971.
16. Lin, J.; Zhong, J.; Zhong, S.; Li, H.; Zhang, H.; Chen, W. Modulating Electronic Transport Properties of MoS_2 Field Effect Transistor by Surface Overlayers. *Appl. Phys. Lett.* **2013**, *103*, 063109.
17. Spi Supplies. http://www.2spi.com/.
18. Nanoscience Instruments. www.nanoscience.com.
19. Kresse, G.; Furthmuller, J. Efficiency of *Ab-Initio* Total Energy Calculations for Metals and Semiconductors Using a Plane-Wave Basis Set. *Comput. Mater. Sci.* **1996**, *6*, 15–50.
20. Wypych, F.; Weber, T.; Prins, R. Scanning Tunneling Microscopic Investigation of 1T-MoS_2. *Chem. mater.* **1998**, *10*, 723–727.
21. Enyashin, A. N.; Bar-Sadan, M.; Houben, L.; Seifert, G. Line Defects in Molybdenum Disulfide Layers. *J. Phys. Chem. C* **2013**, *117*, 10842–10848.
22. McDonnell, S.; Brennan, B.; Azcatl, A.; Lu, N.; Dong, H.; Buie, C.; Kim, J.; Hinkle, C. L.; Kim, M. J.; Wallace, R. M. HfO_2 on MoS_2 by Atomic Layer Deposition: Adsorption Mechanisms and Thickness Scalability. *ACS Nano* **2013**, *7*, 10354–10361.
23. Wagner, C.; Davis, L.; Zeller, M.; Taylor, J.; Raymond, R.; Gale, L. Empirical Atomic Sensitivity Factors for Quantitative

Analysis by Electron Spectroscopy for Chemical Analysis. *Surf. Interface Anal.* **1981**, *3*, 211–225.
24. Lang, O.; Tomm, Y.; Schlaf, R.; Pettenkofer, C.; Jaegermann, W. Single Crystalline GaSe/WSe_2 Heterointerfaces Grown by Van Der Waals Epitaxy. II. Junction Characterization. *J. Appl. Phys.* **1994**, *75*, 7814–7820.
25. Henrion, O.; Jaegermann, W. Uhv Model Experiments of the Semiconductor/Electrolyte Interface: Adsorption of I_2 on N-and P-Doped WSe_2 (0001). *Ber. Bunsen-Ges. Phys. Chem.* **1998**, *102*, 96–102.
26. Nist X-Ray Photoelectron Spectroscopy Database, Version 4.1; National Institute of Standards and Technology: Gaithersburg, 2012. http://srdata.nist.gov/xps/.
27. Schlaf, R.; Lang, O.; Pettenkofer, C.; Jaegermann, W. Band Lineup of Layered Semiconductor Heterointerfaces Prepared by Van Der Waals Epitaxy: Charge Transfer Correction Term for the Electron Affinity Rule. *J. Appl. Phys.* **1999**, *85*, 2732–2753.
28. Pirkle, A. R.; Chabal, Y. J.; Colombo, L.; Wallace, R. M. *In Situ* Studies of High-K Dielectrics for Graphene-Based Device. *ECS Trans.* **2009**, *19*, 215–224.
29. Gong, C.; Huang, C.; Miller, J.; Cheng, L.; Hao, Y.; Cobden, D.; Kim, J.; Ruoff, R. S.; Wallace, R. M.; Cho, K. Metal Contacts on Physical Vapor Deposited Monolayer MoS_2. *ACS Nano* **2013**, *7*, 11350–11357.
30. Greiner, M. T.; Chai, L.; Helander, M. G.; Tang, W. M.; Lu, Z. H. Metal/Metal-Oxide Interfaces: How Metal Contacts Affect the Work Function and Band Structure of MoO_3. *Adv. Funct. Mater.* **2013**, *23*, 215–226.
31. Grant, A.; Griffiths, T.; Pitt, G.; Yoffe, A. The Electrical Properties and the Magnitude of the Indirect Gap in the Semiconducting Transition Metal Dichalcogenide Layer Crystals. *J. Phys. C: Solid State Phys.* **1975**, *8*, L17.
32. Huisman, R.; De Jonge, R.; Haas, C.; Jellinek, F. Trigonal-Prismatic Coordination in Solid Compounds of Transition Metals. *J. Solid State Chem.* **1971**, *3*, 56–66.
33. Fortin, E.; Sears, W. Photovoltaic Effect and Optical Absorption in MoS_2. *J. Phys. Chem. Solids* **1982**, *43*, 881–884.
34. Späh, R.; Lux-Steiner, M.; Obergfell, M.; Bucher, E.; Wagner, S. N-$MoSe_2$/P-WSe_2 Heterojunctions. *Appl. Phys. Lett.* **1985**, *47*, 871–873.
35. Dolakia, D.; Solanki, G.; Patel, S.; Agarwal, M. Optical Band Gap Studies of Tungsten Sulphoselenide Single Crystals Grown by Dvt Technique. *Sci. Iran.* **2003**, *10*, 373–382.
36. Upadhyayula, L.; Loferski, J.; Wold, A.; Giriat, W.; Kershaw, R. Semiconducting Properties of Single Crystals of N-and P-Type Tungsten Diselenide (WSe_2). *J. Appl. Phys.* **2003**, *39*, 4736–4740.
37. Kautek, W.; Gerischer, H.; Tributsch, H. The Role of Carrier Diffusion and Indirect Optical Transitions in the Photoelectrochemical Behavior of Layer Type D-Band Semiconductors. *J. Electrochem. Soc.* **1980**, *127*, 2471–2478.
38. Splendiani, A.; Sun, L.; Zhang, Y.; Li, T.; Kim, J.; Chim, C.-Y.; Galli, G.; Wang, F. Emerging Photoluminescence in Monolayer MoS_2. *Nano Lett.* **2010**, *10*, 1271–1275.
39. Kim, S.; Konar, A.; Hwang, W. S.; Lee, J. H.; Lee, J.; Yang, J.; Jung, C.; Kim, H.; Yoo, J. B.; Choi, J. Y.; *et al.* High-Mobility and Low-Power Thin-Film Transistors Based on Multilayer MoS_2 Crystals. *Nat. Commun.* **2012**, *3*, 1011.
40. Qin, P.; Fang, G.; Ke, W.; Cheng, F.; Zheng, Q.; Wan, J.; Lei, H.; Zhao, X. *In Situ* Growth of Double-Layer MoO_3/MoS_2 Film from MoS_2 for Hole-Transport Layers in Organic Solar Cell. *J. Mater. Chem. A* **2014**, *2*, 2742–2756.
41. Herrera-Gomez, A.; Hegedus, A.; Meissner, P. L. Chemical Depth Profile of Ultrathin Nitrided SiO_2 Films. *Appl. Phys. Lett.* **2002**, *81*, 1014–1016.
42. Blöchl, P. E. Projector Augmented-Wave Method. *Phys. Rev. B: Condens. Matter Mater. Phys.* **1994**, *50*, 17953.
43. Ceperley, D. M.; Alder, B. J. Ground-State of the Electron-Gas by a Stochastic Method. *Phys. Rev. Lett.* **1980**, *45*, 566–569.